Improved urban flood detection using Sentinel-1 by effective combination of elevation data with image intensity and interferometric coherence

Article

Published Version

Creative Commons: Attribution 4.0 (CC-BY)

Open Access

Mason, D. ORCID: https://orcid.org/0000-0001-6092-6081 and Dance, S. ORCID: https://orcid.org/0000-0003-1690-3338 (2026) Improved urban flood detection using Sentinel-1 by effective combination of elevation data with image intensity and interferometric coherence. Journal of Applied Remote Sensing, 20 (2). 026510. ISSN 1931-3195 doi: 10.1117/1.JRS.20.026510 Available at https://centaur.reading.ac.uk/129182/

It is advisable to refer to the publisher's version if you intend to cite from the work. See Guidance on citing.

To link to this article DOI: http://dx.doi.org/10.1117/1.JRS.20.026510

Publisher: Society of Photo-optical Instrumentation Engineers (SPIE)

All outputs in CentAUR are protected by Intellectual Property Rights law, including copyright law. Copyright and IPR is retained by the creators or other copyright holders. Terms and conditions for use of this material are defined in the End User Agreement.

www.reading.ac.uk/centaur

CentAUR

Central Archive at the University of Reading

Reading's research outputs online

JARS Journal of Applied Remote Sensing

RESEARCH PAPER

Improved urban flood detection using Sentinel-1 by effective combination of elevation data with image intensity and interferometric coherence

David C. Mason[a,b,*] **and Sarah L. Dance**[a,b,c]
[a]National Centre for Earth Observation, Reading, United Kingdom
[b]University of Reading, Department of Meteorology, Reading, United Kingdom
[c]University of Reading, Department of Mathematics and Statistics, Reading, United Kingdom

ABSTRACT. Flooding of urban areas causes great risk to lives and property. It may be detected using high-resolution synthetic aperture radar (SAR) sensors by measuring changes in double scattering and/or interferometric coherence between pre- and postflood images. Double scattering in a postflood image usually increases compared with a preflood image, whereas coherence generally decreases. Less attention has been paid to change detection techniques that use a high-resolution digital surface model (DSM) in addition to double scattering and coherence. The availability of a DSM may enable increased spatial resolution in the flood extent delineation and allow flood depth (useful for flood damage assessment) to be measured as well as extent. We aim to investigate how best to combine double scattering, coherence, and DSM data for urban flood mapping using change detection. Four urban floods from Asia and Europe were studied. Due to the limited training data available in these floods, a shallow learning approach was adopted, using separate training and test datasets. It was found that when classifying using double scattering and coherence only, an approach using a neural network (NN) was marginally superior to an established method. The DSM was applied to the resulting NN classification in a second-stage process. The results indicated that using the NN employing only double scattering and coherence, a weighted average classification accuracy of 84% could be achieved on test data. If the DSM was also included in the classification, the accuracy increased to 91%, spatial resolution improved, and flood depth maps could generally be generated. These findings should be of use in automating the detection of urban flooding as an aid to operational flood incident management and flood forecasting.

© The Authors. Published by SPIE under a Creative Commons Attribution 4.0 International License. Distribution or reproduction of this work in whole or in part requires full attribution of the original publication, including its DOI. [DOI: 10.1117/1.JRS.20.026510]

Keywords: flood incident management; hydrology; synthetic aperture radar; interferometric coherence; digital surface model

Paper 250421G received Jun. 30, 2025; revised Mar. 16, 2026; accepted Mar. 26, 2026; published Apr. 17, 2026.

1 Introduction

Flooding from pluvial, fluvial, and coastal sources is a significant natural hazard that affects people all over the world, causing death, injury, disease, homelessness, displacement, and economic loss.[1] Although the majority of a flood may lie in the rural area, it is in the urban area where the risk to lives and property is greater, as over half the world's population now lives in

---

[*] Address all correspondence to David C. Mason, d.c.mason@reading.ac.uk

Handling Editor: Diego Reale, Associate Editor

cities.[2] More than 13,000 people were killed, and there were economic losses of $187 billion in the ten costliest floods between 1980 and 2014.[3] The heavier rainfall associated with climate change and the growing urbanization of floodplains imply an increased likelihood of flooding in the future, with an increasing proportion of the population becoming exposed to floods.[4,5] There is a clear need to develop near-real-time urban flood mapping capabilities to assist operational flood incident managers and emergency responders.[6] Urban flood extent maps can also be assimilated into flood inundation models to improve their predictions[7,8] and to evaluate the improvements.[9–11]

High-resolution SAR is a powerful tool for the synoptic detection of urban flood extents. Unlike visible band sensors, SAR, being an active sensor, is generally able to penetrate the cloud often associated with flooding and can image at night-time as well as during the day. Several very high-resolution SARs capable of detecting urban flooding are currently providing imagery, including the TerraSAR-X (X-band), ALOS-2/PALSAR-2 (L-band), COSMO-SkyMed (X-band), RADARSAT (C-band), ICEYE(X-band), RISAT (C- and X-band), GaoFen-3 (C-band), and StriX (X-band) constellations. This paper is concerned with the Sentinel-1 (S-1) C-band constellation, which has the advantage that it provides the user with an open-access product of high (10 m) resolution data available in processed multilook georegistered form 1 h after acquisition at the ground station.[12] The two-satellite constellation can give a temporal resolution of 6 days at the equator and higher at higher latitudes. Although other SAR constellations can provide higher temporal resolution, S-1's Interferometric Wide (IW) Mode, the primary one over land, offers a large 250-km swath width, making it well-suited for flood detection as it covers extensive areas efficiently. In addition, the S-1 Global Flood Monitoring (GFM) product now provides probabilistic flood extents in rural areas in near real-time for all S-1 scenes acquired globally, although urban areas are currently masked out.[13]

Synthetic aperture radar (SAR) is fundamentally a side-looking imaging technique, which allows measurements along the range (across-track) dimension to complement those along the azimuth (along-track) dimension. As a result, in urban areas, SAR causes strong double scattering (double bounce) because the man-made vertical structures (building walls) and their adjacent horizontal surfaces (ground, roads) form highly efficient corner reflectors, causing strong radar signals back at the sensor.[14] The buildings also cause Radar shadowing and layover, so that substantial areas of the urban ground surface may not be visible to the SAR. These factors cause difficulty in developing automatic methods to map urban flooding using SAR. However, a variety of techniques have been developed, including analysis of backscatter in a postflood SAR image,[15–18] analysis of change in backscatter between pre- and postflood SAR images,[19–24] use of interferometric coherence together with intensity backscatter in pre- and postflood SAR images[25–35] and multitemporal analysis of SAR images.[36–38] These techniques have been reviewed in Ref. 39. Here, we are concerned with the subclass of these methods involving change detection between pre- and postflood images, first introduced in Ref. 19.

Double scattering in a postflood image between suitably oriented buildings and floodwater should generally exceed that in a preflood image, where double scattering is between the buildings and the unflooded ground.[20] Because double scattering is the dominant scattering method in the urban area, if the ratio of the postflood to preflood brightness is greater than 1, the pixel is likely flooded (assuming shallow flooding), whereas if it is ∼1 the pixel is probably not flooded. Furthermore, several change detection studies have investigated ways of combining brightness ratio with interferometric coherence to detect flooding in urban areas.[25–35] An unflooded urban area should display high coherence between post- and preflood images, whereas if the area is flooded, the coherence should be low. These change detection studies are reviewed in Sec. 2.

Less attention has been paid to change detection techniques that use a digital surface model (DSM) in addition to brightness and coherence. Section 2 also reviews previous work in this area. The availability of a DSM may allow increased spatial resolution in the flood extent delineation and also the use of the additional hydrodynamic constraint that flood surfaces should be locally flat, so that flood depth may be measured as well as extent. Flood depth is useful for flood damage assessment. Combining flood depth with flood depth-damage curves is a common method for assessing the economic losses caused by floods, which is important for insurance purposes and disaster relief planning.[40] Unfortunately, it is difficult to obtain open-source DSM data with similar resolution to that of Sentinel-1 over large areas of the globe. The Copernicus DEM EEA-10 10 m DSM (derived from WorldDEM data) is now available open-source over Europe, but to a restricted range of research users.[41] The Copernicus DEM GLO-30 30 m DSM is available open-source globally, but is generally of too low a resolution to contain sufficient structure in urban areas. It should also be noted that, while regional rather than global, many developed countries have constructed very high-resolution LiDAR DSM datasets of urban areas, which may be open-source, as in the UK.[42]

The object of the paper is to investigate how best to combine double scattering, interferometric coherence, and high-resolution digital elevation data when the change detection technique is used for urban flood mapping. The main contribution and novelty of our research is to improve urban flood detection by combining the discriminatory power of double scattering and coherence with the higher resolution DSM data, to increase the spatial resolution of the flood extent and allow flood depth measurement.

The structure of the paper is as follows. Section 2 discusses the literature on this topic. Section 3 considers relevant theory regarding urban flood detection using double scattering and coherence. Section 4 introduces the flood events studied and their associated data sets. Section 5 considers the development of the classification strategy. Section 6 presents the results derived using this strategy. A discussion is provided in Sec. 7 and conclusions in Sec. 8.

2 Related Work

The majority of change detection studies have investigated how the brightness ratio and interferometric coherence can complement each other in detecting urban flooding.[25–35] Reference 25 was the first to show that the use of coherence in conjunction with SAR intensity considerably reduced classification error in flooded urban areas compared with using intensity alone, using COSMO-SkyMed images. Reference 26 detected a flooded urban area at first approximately using double-scattering from flooded buildings that were roughly parallel to the Sentinel-1 satellite flight direction, then improved this initial estimate based on the change in coherence between pre- and postflood images. Reference 27 detected urban flooding by combining Sentinel-1 intensity and coherence using a Bayesian network framework with unsupervised classification. Reference 28 performed urban flood mapping of TerraSAR-X intensity and coherence using an active self-learning neural network. While Refs. 26–28 were based on data of Hurricane Harvey in Houston in 2017, Ref. 29 investigated numerous urban flood mapping approaches, including change detection and coherence using Canadian flood events, and Ref. 30 used intensity and coherence of Indonesian floods to study urban flooding. Reference 31 studied Sentinel-1 data of a flood in Iran and combined intensity and coherence into a single measure of urban flooding that was superior to one based on intensity alone. Reference 32 showed that urban flood water detection could be improved by detecting a change in coherence from both co- and cross-polarized SAR images and considered not only double scattering but also multiple scattering from buildings. Reference 33 input dual-polarization Sentinel-1 multitemporal intensity and coherence information into a deep convolutional neural network with an urban-aware model to improve urban flood mapping. Reference 34 also employed deep learning for urban flood detection, feeding intensity, and coherence information into a convolutional Siamese network. Reference 35 developed a Sentinel-1 benchmark dataset for urban and open area flood mapping and investigated state-of-the-art convolutional neural networks for segmenting urban and open flood areas. It was concluded that these were currently limited, partly by the constraint of a small training dataset. In addition, Refs. 36–38 detected urban flooding using coherence alone. A key finding from these studies is that using coherence in conjunction with the brightness ratio considerably reduces urban flooding classification error compared to using the brightness ratio alone.

References 25–38 detected urban flooding principally using SAR data to estimate the brightness ratio and coherence. However, as explained in Sec. 1, there are advantages in employing a DSM to complement the SAR data. Less attention has been paid to change detection techniques that use a DSM as well as brightness and coherence for urban flood detection. In addition to Ref. 21, Ref. 29 tested urban flood mapping approaches from satellite and *in situ* data of Canadian flood events, Ref. 43 investigated the dependence of the brightness ratio on building orientation using LiDAR data, and Ref. 44 used a DSM in conjunction with double scattering and coherence to aid in the detection of deeper floods.

The present study builds on the above research by investigating how best to combine elevation data with double scattering and coherence to improve urban flood mapping when using change detection.

3 Urban Flood Detection Using Double Scattering and Interferometric Coherence

This section introduces the theory of double scattering and coherence underlying the measurement of the double scattering brightness ratio and the coherence ratio, prior to their use in the development of the classification strategy.

Suitably oriented buildings generally cause significant double scattering not only because a substantial proportion of the incoming radiation is reflected back to the sensor but also because the paths of the double scattering rays striking the building wall all have the same length, namely the slant range of the base of the wall.[45]

The theoretical background of the use of double scattering for urban flood detection assuming a change detection technique that uses preflood and postflood images is outlined in Ref. 43 and is only summarized here. Assuming that the ground between the buildings is flooded to only a small depth compared with the building heights and that the double scattering cross-sections in the post- and preflood images are σ^0_{post} and σ^0_{pre} respectively, the post- to preflood brightness ratio r

$$r = \sigma^0_{\mathrm{post}}/\sigma^0_{\mathrm{pre}}, \tag{1}$$

is higher than 1 mainly because the permittivity of water is greater than that of asphalt (Table 1, Ref. 17). On the contrary, for ground that is not flooded, r should be ~ 1.

In previous studies, VV polarization has been shown to be better than VH at distinguishing flooded from nonflooded double scatterers, and only VV data were used.[31,43] For copolarized data, modelling indicates that double scattering is strongest when the building wall is parallel with the satellite travel direction, when the angle φ between their directions is zero, and falls off rapidly for $\varphi > 10$ deg, suggesting that few double scatterers might be detected in an urban area.[25] However, for Sentinel-1 VV data, it has been shown that the modelling tends to underestimate the number of double scatterers having large brightness ratios in the φ range 10 deg to 30 deg.[43] Double scattering may also fall off if flooding is deep, in which case little building wall height may remain above the floodwater to cause double scattering.[44]

Interferometric coherence is used as an adjunct to the brightness ratio to discriminate between flooded and nonflooded areas. The interferometric coherence at a pixel is computed from N pixels neighbouring the pixel taken from a pair of complex SAR images, S_1 and S_2, and is expressed as

$$\gamma = \frac{|\sum_{i=1}^{N} S_{1i} S_{2i}^{*}|}{\sqrt{(\sum_{i=1}^{N} |S_{1i}|^2 \sum_{i=1}^{N} |S_{2i}|^2)}}. \tag{2}$$

In urban areas, two images having the same sensor parameters acquired prior to the flood (pre-event pair) will generally show high coherence owing to their similarity. On the contrary, if one of the images contains flooding (co-event pair), coherence will generally be lower because

Table 1 Urban flood events and dates.

Event site	Country	Event date
Aqqala	Iran	March 2019
Koriyama	Japan	October 12 to 13, 2019
Iwaki	Japan	October 12 to 13, 2019
Blessem	Germany	July 15 to 18, 2021

the changes between the images cause decorrelation. A coherence of 1 indicates fully correlated data, and 0 fully uncorrelated. Coherence has the advantage that it is independent of building orientation with respect to the satellite travel direction, unlike double scattering, which falls off with increasing φ angle.[38] This makes it a useful feature to combine with double scattering. However, it is a local area measure, whereas the brightness ratio is pixel-based and consequently has higher spatial resolution.

Three Sentinel-1 VV images $t1$, $t2$, and $t3$ having the same pass and incidence angle are required by the method, with $t1$ and $t2$ being acquired before flooding and $t3$ during flooding. The double scattering brightness ratio r is

$$r = \sigma^0_{t3}/\sigma^0_{t2}, \tag{3}$$

and the interferometric coherence ratio coh_rat $(0 < coh\_rat \leq 1)$ is

$$coh\_rat = \gamma_{t2\ t3}/\gamma_{t1\ t2}, \tag{4}$$

where σ^0_{t3} and σ^0_{t2} are the linear backscattering cross-sections of $t3$ and $t2$ and $\gamma_{t2\ t3}$ and $\gamma_{t1\ t2}$ are the coherences between $t2$ and $t3$ (co-event pair), and $t1$ and t2 (pre-event pair), respectively.

4 Study Events and Datasets

Four urban floods from Asia and Europe were studied: Aqqala, Iran; Koriyama, Japan; Iwaki, Japan; and Blessem, Germany (Table 1).

a. Aqqala
Golestan Province in North-East Iran [Fig. 1(a)] experienced severe flooding during March 2019. The city of Aqqala in Golestan, situated on the Gorganrood river, was one of the worst-affected urban areas.[31,47] Excellent validation data were available in the form of a Jilin-1 0.9-m resolution multispectral image [Fig. 1(b)] acquired on the same day as the postflood Sentinel-1 image (Table 2). Figure 1(c) shows aerial photographs of the urban flooding,[46] and Fig. 1(d) shows the urban extent of Aqqala. Figure 1(e) shows the thresholded Normalized Difference Water Index (NDWI) image derived from Fig. 1(b) that was used for validation, using a threshold value of 0.06 to distinguish flooded from unflooded urban pixels.[48,49]

b. Koriyama
Typhoon Hagibis caused unprecedented rainfall across a third of Japan [Fig. 2(a)] on 12th to 13th October 2019. The typhoon was extremely powerful, and the heavy rainfall resulted from

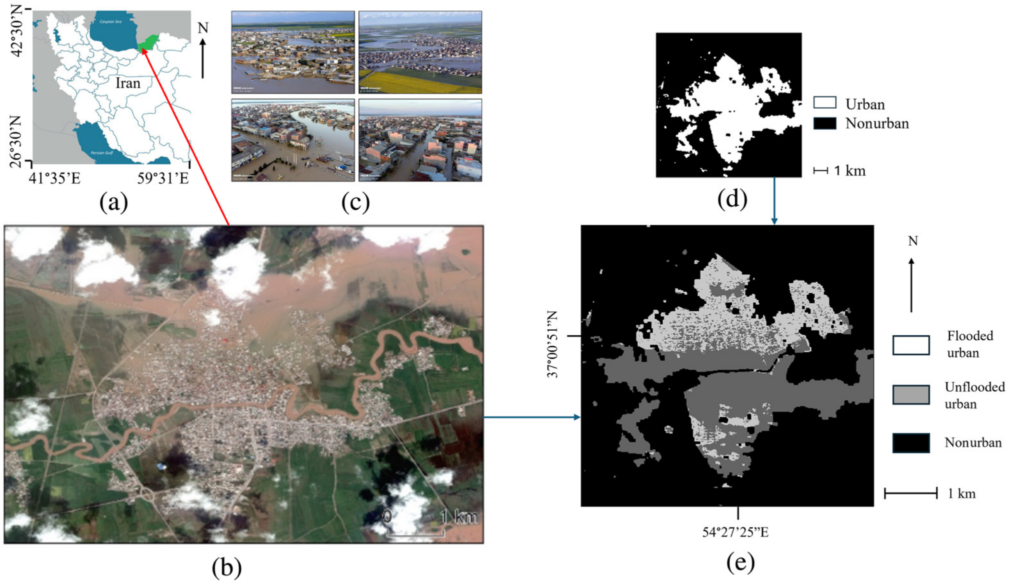

Fig. 1 (a) Golestan Province (green), Iran, (b) Jilin-1 multispectral image of March 29, 2019, (c) aerial photos of the flooding,[46] (d) Aqqala urban extent, and (e) thresholded NDWI image.

Table 2 Sentinel-1 IW VV/VH images used for flood detection (UTC, Coordinated Universal Time).

Test site	Aqqala		Koriyama		Iwaki		Blessem	
Data type	Postflood image	Preflood image	Postflood image	Preflood image	Postflood image	Preflood image	Post-flood image	Pre-flood image
Intensity (GRD images)	Mar 29, 2019; 14:20 UTC	Mar 17, 2019; 14:20 UTC	Oct 12, 2019; 20:42 UTC	Oct 6, 2019; 20:43 UTC	Oct 12, 2019; 20:42 UTC	Oct 6, 2019; 20:43 UTC	Jul 16, 2021; 05:42 UTC	Jun 22, 2021; 05:42 UTC
Coherence (SLC images)	Mar 29, 2019; 14:20 UTC	Mar 17, 2019; 14:20 UTC	Oct 12, 2019; 20:42 UTC	Oct 6, 2019; 20:43 UTC	Oct 12, 2019; 20:42 UTC	Oct 6, 2019; 20:43 UTC	Jul 15, 2021; 05:51 UTC	Jul 3, 2021; 05:51 UTC
		Mar 5, 2019; 14:20 UTC		Sep 24, 2019; 20:43 UTC		Sep 24, 2019; 20:43 UTC		Jun 21, 2021; 05:51 UTC

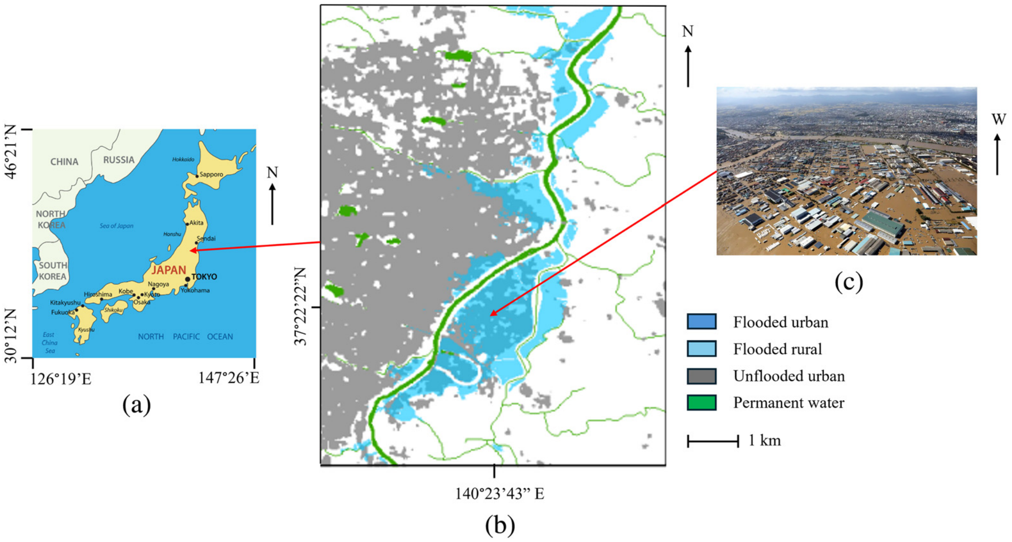

Fig. 2 (a) Japan, (b) reference map of the Koriyama flooding on October 13, 2019,[50] and (c) aerial photo of the main urban area flooded (viewed from the east, showing the Abukuma river).[51]

the large volume of warm air it carried.[52] The city of Koriyama in Fukushima Prefecture was badly affected, with thousands of buildings flooded.[53] The Geospatial Information Authority of Japan (GSI) published a reference map of the Koriyama flooding based on data collected up to 13th October [Fig. 2(b)].[50] A Sentinel-1 overpass imaged the flooding on the 12th of October (Table 2). Figure 2(c) shows an aerial photograph of the main urban area flooded, taken just a few hours after the SAR overpass.[51] The south of the flooded area largely contains houses, whereas in the north is a trading estate that was quite deeply flooded.

c. Iwaki

The city of Iwaki, about 100-kms south-east of Koriyama [Fig. 3(a)], also experienced severe flooding during Typhoon Hagibis. A flood inundation map of the flooding that occurred on the 12th and 13th of October was released by Iwaki City Council [Fig. 3(b)].[54] The map was developed by local officers through field reconnaissance. It was regarded as preliminary, but no updated map has been published to date.[38] Although the map has been used below for validation, it must be treated with caution as it maps the maximum flood

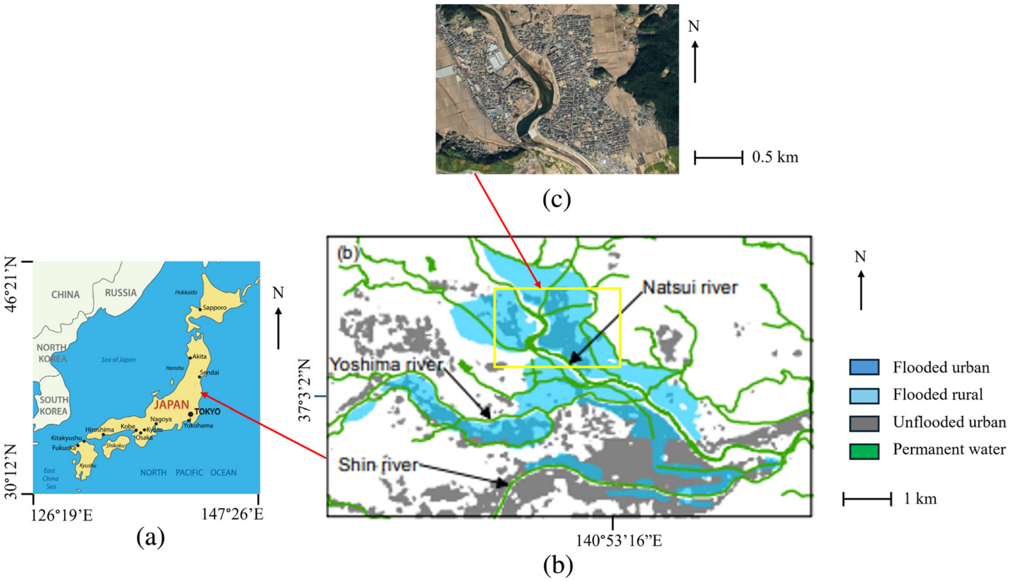

Fig. 3 (a) Japan, (b) reference map of the Iwaki flooding on October 13, 2019[54] (yellow rectangle indicates area of analysis), and (c) aerial photo of unflooded buildings in the yellow rectangle.[55]

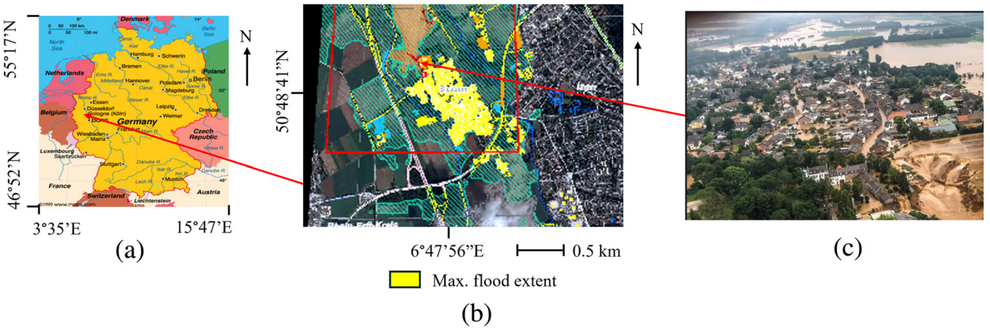

(a)
(b)
(c)

Fig. 4 (a) Germany, (b) maximum flood extent of the Blessem flooding on July 15 to 16,[56] and (c) aerial photo of the flooding viewed from the North of Blessem looking South.[57]

extent over the 2-day period. The flooded housing estates in the north of the image [yellow rectangle, Fig. 3(b)] seem to be detected in the SAR images (see below), whereas the flooding near the confluence of the Natsui, Yoshima, and Shin rivers seems not to be. This discrepancy has been noted in Ref. 38. It is likely that the flood wave progressed further downstream between the SAR acquisition date (Oct 12, 2019) and the validation date (Oct 13, 2019) (Table 2). As a result, the analysis below has been limited to the content of the yellow rectangle in the flood inundation map [Fig. 3(c)[55]].

d. Blessem

Severe flooding affected several European countries in July 2021 and led to loss of life and significant damage to property, particularly in Germany [Fig. 4(a)]. Blessem, a village on the river Erft near Cologne, was one of many towns and villages affected.[57] The peak of the flooding was on the 15th of July, when floodwater inundated a quarry causing a major landslide. A Sentinel-1 overpass imaged the flooding on the 16th of July (Table 2). An estimate of maximum flood extent was provided by the Copernicus Emergency Management Service using a multispectral image from the 18th of July, past the flood peak [Fig. 4(b)].[56] However, this was not necessarily the flood extent at the time of SAR overpass on the 16th of July at 05:42, and instead, an aerial photo taken on the 15th of July was used to provide validation [Fig. 4(c)].[57]

The European Space Agency (ESA) SNAP toolbox was used to apply several preprocessing steps to the level-1 SAR Interferometric Wide Swath (IW) images (Fig. 5). For the ground range detected (GRD) intensity images, image subsetting, orbit correction, radiometric calibration, and range-Doppler terrain correction were applied [Fig. 5(a)]. The pre- and postflood intensity images produced were collocated to the DSM in the WGS84 coordinate system. For the single look complex (SLC) images, image coherence was extracted for each image pair using a processing sequence involving image subsetting, orbit correction, back geocoding, enhanced spectral

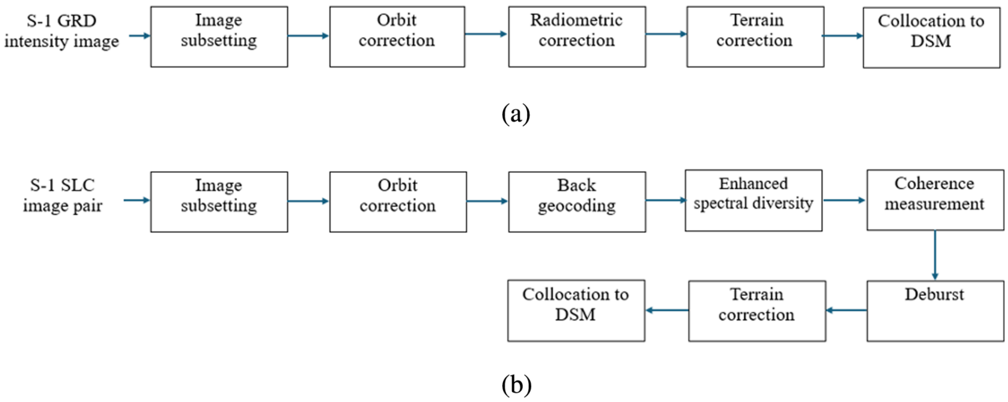

(a)
(b)

Fig. 5 Preprocessing steps applied to the Sentinel-1 (S-1) images. (a) GRD intensity image preprocessing and (b) SLC image pair preprocessing to estimate coherence (after Ref. 44).

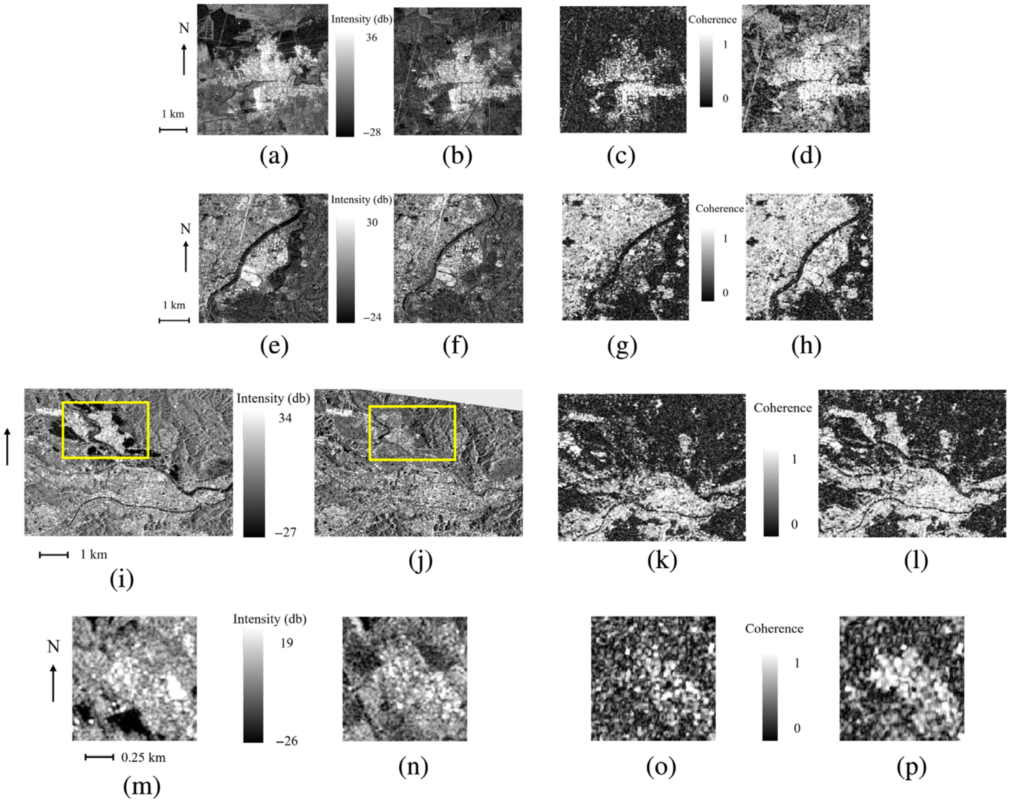

Fig. 6 Sentinel-1 VV post- and preflood intensity images, and coherence images for the co-event image pair and pre-event image pair, for Aqqala [(a)–(d) respectively, see study area in Fig. 1(e)], Koriyama [(e)–(h), see Fig. 2(b)], Iwaki (yellow rectangles indicate analysis area) [(i)–(l), see Fig. 3(b)], and Blessem [(m)–(p), see Fig. 4(b)].

diversity, coherence measurement (using a 70-m square window), deburst, and range-Doppler terrain correction [Fig. 5(b)].[58]

Figure 6 shows, for all four test sites, the Sentinel-1 VV postflood and preflood intensity images, and the coherence images for the co-event image pair and pre-event image pair.

The urban areas of the test sites were identified using the World Settlement Footprint (WSF) 2019 10-m resolution dataset.[59]

Figure 7 shows the brightness ratio and coherence ratio averaged over the coherence window size (7 × 7 pixel) and masked by the urban area, for all the sites. These were derived from the intensity and coherence images of Fig. 6. In Fig. 7, it can be seen that the average brightness ratio and coherence ratio are negatively correlated.

5 Development of Classification Strategy

This section considers the question of how best to combine brightness ratio, coherence ratio, and digital elevation data for urban flood detection.

In previous work, we have detected, urban flooding using single-pixel double scatterers (DS) at building edges that were aligned roughly parallel to the satellite direction of travel, so that double scattering was high for these DS.[21,43,44] In this, the WorldDEM DSM was used to find the orientations of these DS together with their heights. However, it became apparent from the test set that the density of DS was generally much lower than the density of pixels of high brightness ratio. The low DS density was due to there being insufficient resolution in the DSM to resolve individual buildings. DS were tending to be detected at the beginning and end of streets of houses, even though the individual houses along the streets were causing high double scattering. As a result, it was decided to detect regions of high brightness ratio scattering rather than individual DS.

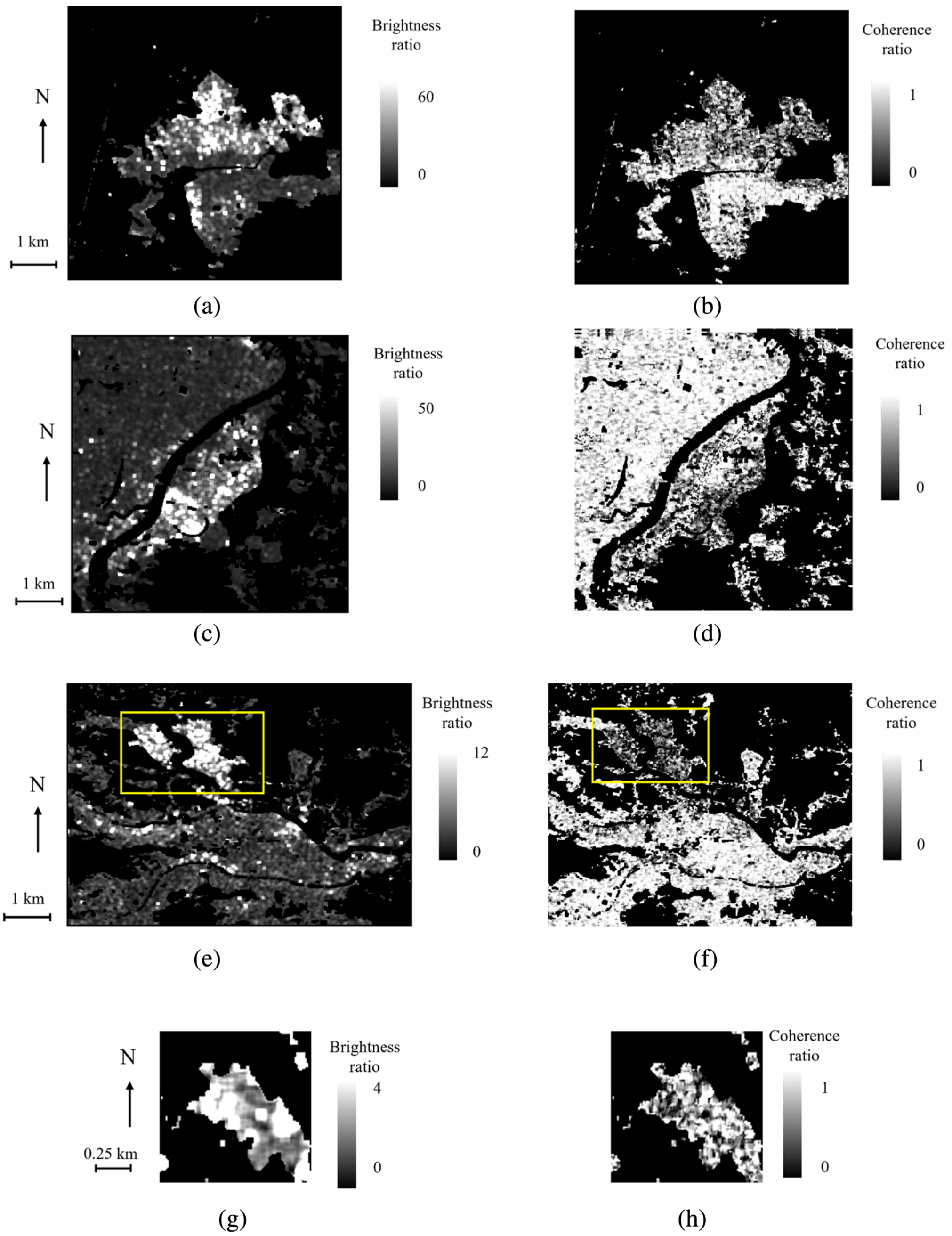

Fig. 7 Average brightness ratio and coherence ratio masked by the urban area, for Aqqala (a), (b), Koriyama (c), (d), Iwaki (yellow rectangles indicate analysis area) (e), (f), and Blessem (g), (h).

This changes the role of the DSM. Instead of being used to detect individual DS, it is now used to provide increased resolution compared with that of the small areas of flooding detected and may also allow an estimate of flood depth to be made from the flood extent. Knowledge of the flood depth at a point allows better assessment of building damage there.

5.1 Urban Flood Index

Reference 31 found that urban flooding caused an increase in brightness ratio and a decrease in interferometric coherence, with VV polarization being more sensitive than VH. The authors introduced the urban flood index (UFI) as a measure of flooding over a small urban area. Urban flood index is a ratio formed by dividing the average brightness ratio over the area by the coherence ratio, using VV polarization.

$$\mathrm{UFI} = \bar{r}/coh\_rat. \tag{5}$$

Urban flood index should be high if the area is flooded, and low (close to 1) if not. A threshold *ufi_thresh* is used to discriminate between flooded and unflooded classes. The size of the small urban area used to determine UFI was taken as the size of the window used for coherence measurement (70 × 70 m).

The method is able to detect regions of low average brightness ratio (e.g., a building flooded to a substantial proportion of its depth) as flooded, provided the region also has a low coherence ratio (which is likely in this example), as the UFI value may then still exceed the threshold. However, the UFI is a 1D measure, whereas a measure employing the brightness ratio and the coherence ratio as independent variables in a 2D space may be more discriminative. Below, we use the UFI method as a baseline against which others are compared.

5.2 Experiments on Urban Flood Detection Using Compact Networks

References 33–35 have used deep learning techniques for SAR flood detection in both urban and rural areas. These require the estimation of enormous numbers of weights in their convolutional neural networks (CNNs) and hence substantial training data.

In this study, only limited training data were available, which restricts the number of weights that can be estimated. To cope with the limited training data, we have simplified the problem considered in the above studies so that we have only attempted to detect flooding in the urban area, which we assume is represented accurately by the WSF 2019 data.

Reference 60 used a compact CNN network with only 1 hidden C layer to successfully perform SAR image land cover classification. The authors argued that labeled data may be scarce, so that compact CNNs are better than deep CNNs because far fewer weights need to be estimated. Because of its compact configuration, their approach can also process small image patches, giving increased resolution, which is not possible using deep learning techniques.

On the basis of this, given that a fully connected network is a basic component of a CNN, we carried out an experimental study using a bottom-up approach starting with a simple neural network (NN) to detect urban flooding, prior to considering adding more complexity within the constraints set by our limited training data.

We tested an NN two-class classifier with a two-node hidden layer. The latter was necessary as the brightness ratio and coherence ratio are not linearly separable. An NN needs its inputs to be normalized so that their values lie on similar scales. This is often achieved by normalizing using their means and standard deviations. *coh_rat* is already normalized in the range 0 to 1. However, r is not normalized, although it is always positive. r was normalized so that $0 < r < 1$ using

$$r- > \min(r/ratio\_\mathrm{lim},\ 1). \tag{6}$$

It turned out that little accuracy was lost in classifying using r and *coh_rat*, and normalizing r and *coh_rat* in this manner, rather than using their means and standard deviations. Values of *ratio_lim* of 5, 7, and 10 were tested. We adopted the value *ratio_lim* = 10 as this gave the best result, although the results were fairly insensitive to the value of *ratio_lim*.

The NN was trained by scanning the normalized r and *coh_rat* images using 7 × 7-pixel nonoverlapping windows to reduce correlations, with all pixels in a window required to lie in the urban area. Windows having low (< -11 db) average preflood double reflection were ignored, as they were unlikely to be strong double scattering regions. The averages of r and *coh_rat* in each window accepted were input to a Stochastic gradient descent algorithm, together with the validation class of the central pixel in the window, and the window was classified into flooded or unflooded (Fig. 8). A sigmoid activation function was applied to the output of the hidden layer to ensure that the classification output lay in the range 0 to 1. A binary cross-entropy loss function was used in training the NN, as this has been shown to be better for a two-class classifier because it strongly penalizes poor predictions.[61] From experiments, a learning rate of 0.1 with a momentum of 0.9 was found appropriate, with learning converging in less than 10,000 epochs.

Data from the Aqqala and Koriyama sites were used for training the network, as equal numbers of flooded and unflooded samples were available at these sites: 80% of the data were used for training and 20% for subsequent testing. There were 620 training set samples for Aqqala, and 495 for Koriyama, which were combined into a single model with 1115 training set samples.

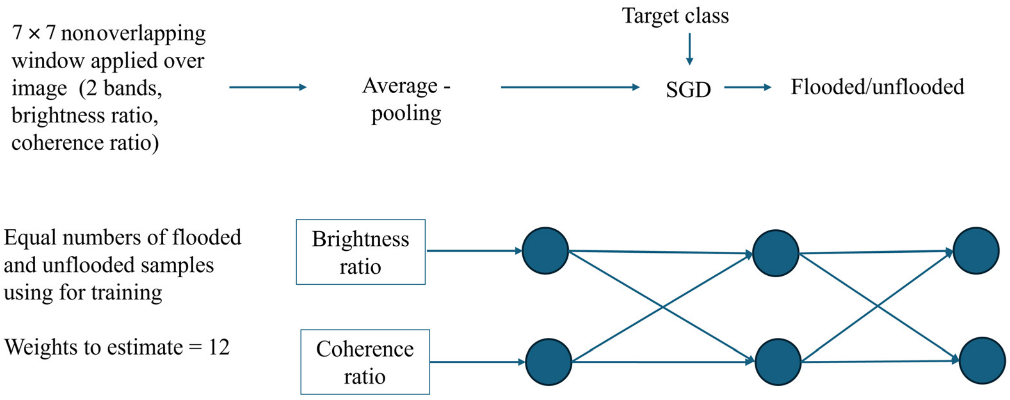

Fig. 8 Neural network 2-class classifier.

Table 3 Classification of test datasets using NN with brightness ratio and coherence ratio.

Site	Training set size	Test set size	Test set flooded: unflooded sample ratio	Test set accuracy (using combined AK model)	True flooded rate (recall)	False flooded rate
Aqqala	620	156	1:1	0.85	0.82	0.13
Koriyama	495	124	1:1	0.90	0.83	0.05
Iwaki	0	241	1:0.05	0.85	0.86	0.45
Blessem	0	33	1:1.2	0.76	0.75	0.24

Table 3 shows the results of classifying the test data sets at the four sites using the combined AK model. Good classification accuracies were achieved for the Aqqala, Koriyama, and Iwaki floods, and the accuracy was still reasonable for the smallest flood at Blessem. This demonstrates the generality of the model, as it was trained on two events to classify further events that were not in the training data, as well as test data from Aqqala and Koriyama.

It should also be advantageous to use *dsm* as a third input to the NN, as the *dsm* height at the window center should be correlated with whether or not the central pixel is flooded. Unfortunately, a problem may arise when normalising *dsm*. In the supervised classification situation, to equalize flooded and unflooded class numbers, it is often possible to simply subsample the major class, as for Aqqala and Koriyama. Then, normalization of *dsm* using mean and standard deviation improves the classification compared with just using r and *coh_rat*. Essentially, negative values of normalized *dsm* are flooded, whereas positive values are unflooded.

However, in the more usual case where no validation data is available, there is no guarantee that classes will be balanced. An example is the severe class imbalance for the Iwaki housing estates, where there are almost no unflooded urban samples. It is not possible to classify using normalized *dsm* in this case. Samples with normalized *dsm* values that are positive tend to be classified as unflooded when they should be flooded. Again, when there is little flooding in an urban area (as is often the case), the dominant class is unflooded, so normalization of *dsm* using mean and standard deviation is again inappropriate.

We also examined a method that used *dsm* differences rather than *dsm* absolute values, to avoid the *dsm* normalization problem. We used not only normalized r and *coh_rat* inputs but also a spot detector in the *dsm* channel. The normalized 3 × 3-pixel spot detector (-0.1, -0.1, -0.1, -0.1, 0.8, -0.1, -0.1, -0.1, -0.1) is applied at the central pixel in the window and is likely to give low values when the central DSM pixel in the window is at low height compared with the surrounding pixels (e.g., in the street), and high values when the central pixel is higher (e.g., on a building roof). However, this had little effect on the accuracy when tested for Aqqala.

A natural extension of using a spot detector in a NN is to use a CNN with a single C layer applying convolutions to the DSM prior to the NN. This would allow the CNN to choose the best

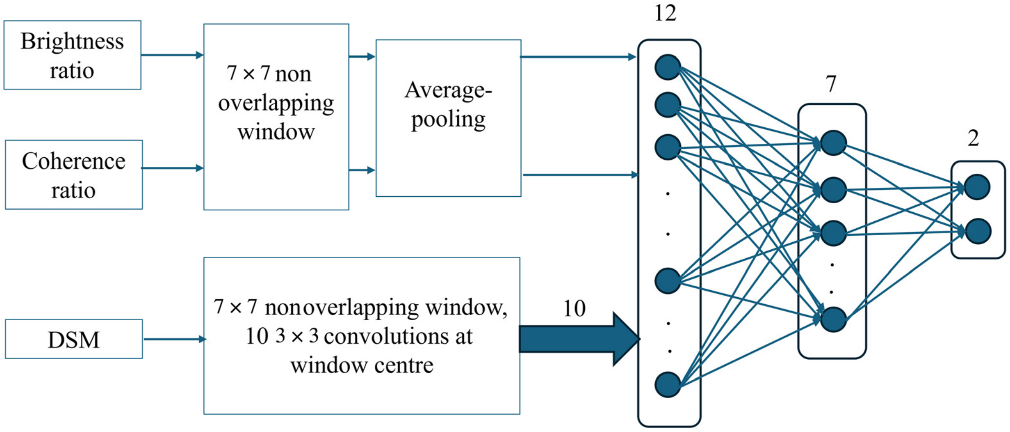

Fig. 9 CNN 2-class classifier.

Table 4 Classification of test data sets using CNN with brightness ratio and coherence ratio.

Site	Training set size	Test set size	Test set flooded: unflooded sample ratio	Test set accuracy (using combined AK model)	True flooded rate (Recall)	False flooded rate	Test set accuracy using NN (and combined AK model)
Aqqala	620	156	1:1	0.85	0.82	0.11	0.85
Koriyama	495	124	1:1	0.90	0.90	0.09	0.90
Iwaki	0	241	1:0.05	0.82	0.83	0.55	0.85

3 × 3 kernel(s) to distinguish flooded from unflooded pixels, giving the advantage that the CNN would be performing the feature extraction from the DSM as well as the overall classification. This is similar to the compact CNN network used in Ref. 60 to perform SAR image classification.

We used a CNN with *dsm* convolved to produce 10 output channels (Fig. 9). Only *dsm* was passed through the convolution layer prior to input to the NN section, with the convolution results being selected at the central pixel in the 7 × 7 window. r and *coh_rat* inputs to the NN were still their averages over the window. This gave 12 input channels to the fully connected network, with the NN having seven hidden-layer neurons and two output neurons. This meant that 147 weights needed to be estimated rather than the 12 weights needed for the simple NN inputting r and *coh_rat*.

The CNN results for Aqqala and Koriyama are very similar to the NN results, using the combined Aqqala/Koriyama model for classification (Table 4). However, Table 4 also considers the example of Iwaki, where the classes are very unbalanced and where the CNN results are worse than the NN results. The Pytorch convolution software used does not initialise its kernel weights so that they sum to zero. This is the normal approach used in computer vision, so that the convolution is sensitive to local variations in brightness, but not to the absolute level of brightness (or in this case *dsm* height). As a result, classifications are sensitive to absolute sample height, which may cause misclassification when classes are unbalanced.

5.3 Two-Stage Urban Flood Detection

It appeared that the potential of the DSM could not be properly exploited by using it as a direct input to the NN or CNN because of the difficulty of normalising *dsm* when classes were unbalanced. An alternative strategy was considered of first classifying on the basis of r and *coh_rat* using the NN and then applying the DSM to the resulting classification in a second-stage process that avoided the DSM normalization problem. One of our objectives is to compare the NN model with the baseline UFI method, which does not use a DSM. Therefore, an additional advantage of this strategy is that it allows the classifications of the NN and UFI methods to be compared at the end of the first stage, then the results of the better classification can be selected for use in the second stage process employing the DSM.

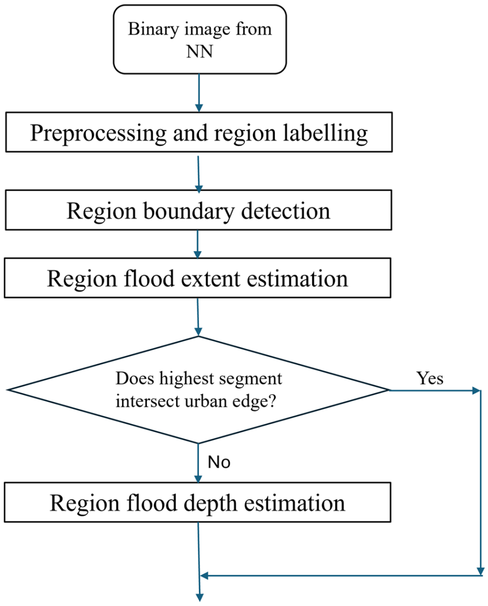

Fig. 10 Second stage processing using DSM.

The second-stage process involves performing a simple segmentation of the flooded regions in the better classification, in which the segmentation is controlled by the DSM values (Fig. 10). In contrast to the low-resolution classifications discussed above, the whole image is first classified at the full 10 m resolution, using adjacent 7×7 windows that are overlapping, with a stride of 1. The resulting classification is processed by the region segmenter. The segmenter processing chain is –

- Flooded regions are eroded to remove noise. Morphological closing using dilate/erode operations is performed to reduce holes within regions and smooth boundaries.
- Flooded regions are labeled, retaining regions >100 pixels so that small floods can be handled. At this stage, a full-resolution image classified using r and coh_rat is available.
- For each flooded region, the region boundary is found.
- The boundary is intersected with the DSM to estimate flood levels at the boundary. Boundary pixels in the DSM will be a mix of heights from ground and buildings, and we want an estimate of the former. The boundary is divided into contiguous segments up to 100 pixels long. For each segment, a histogram of heights along the segment is constructed, and the 20th percentile height (i.e., that at which 20% of heights are below) is calculated. This is an estimate of the mean DTM height along the segment while suppressing higher heights due to buildings. The mean height (dsm_thresh) of the highest boundary segment is found. Pixels of height $< dsm\_thresh$ within the region are set to flooded.
- A check is made on whether the highest boundary segment intersects the edge of the urban area to a significant extent. The flood water on the boundary will only be at zero depth if it lies within the urban zone. If not, the mean height may be an underestimate of the flood height in the region, as water may be flowing in from the adjacent rural area.
- If the highest boundary segment does not intersect the urban edge, the depth of flooding in the region is estimated by subtracting the DSM from the corresponding pixel heights in this flood map, assuming that the flood level over the region is constant. A flood depth map is useful for assessing flood damage.
- If this is not so, water may be flowing in from outside the urban area, and in this case, only the region flood extent is estimated and not the flood depth.

For completeness, Fig. 11 gives an overview of the processing steps involved in classification at (a) full resolution using normalized brightness ratio, coherence ratio, and DSM values and (b) low resolution (sampled at full resolution) using normalized brightness ratio and coherence ratio

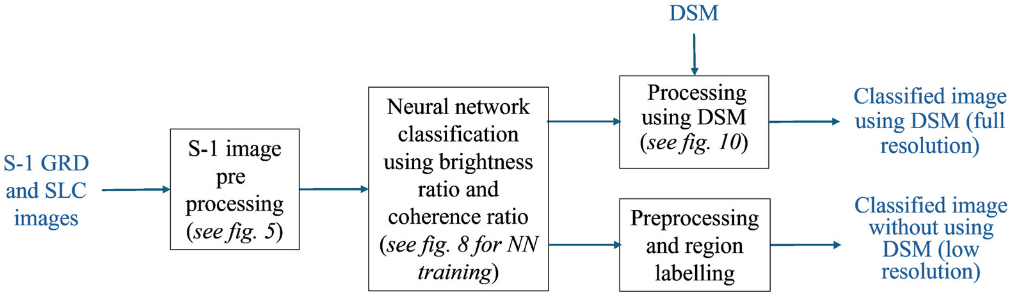

Fig. 11 Overview of the processing steps involved in classification at full and low resolution. This should be viewed in conjunction with Figs. 5, 8, and 10.

but no DSM values. Figure 11 should be viewed in conjunction with Fig. 5 (the preprocessing steps applied to the Sentinel-1 images), Fig. 8 (the neural network two-class classifier training), and Fig. 10 (the second-stage processing using DSM).

6 Results

6.1 Comparison of UFI and NN Methods Using Brightness Ratio and Coherence Ratio

The UFI is an established method of detecting urban flooding using brightness ratio and coherence ratio, but not using a DSM.[31] We compared the UFI method with the NN model using *r* and *coh_rat*. The better of these methods was then used in the second stage process employing the DSM.

In developing the NN model, the data from Aqqala and Koriyama were used to develop the combined AK model (Table 3), as these have balanced classes. The same approach was used to estimate the threshold *ufi_thresh* used in the UFI method. Using 7×7-pixel nonoverlapping windows, it was found that the Aqqala test set accuracy was maximum for $ufi\_thresh = 2.8$, whereas the Koriyama test set accuracy maximized when $ufi\_thresh = 3.2$. As a result, given the similarity of their test set sizes, $ufi\_thresh = 3.0$ was chosen for the combined Aqqala and Koriyama data.

The test set accuracies for the UFI and NN methods were then compared for the Aqqala and Koriyama sites, as these have balanced classes. Table 5 shows that NN gives slightly better classification accuracies than UFI, although the difference is small. UFI is a 1D measure, a simple ratio of *r* and *coh_rat*, whereas the NN method of combining *r* and *coh_rat* is 2D and may extract information slightly more effectively.

6.2 Improvement in Classification Using the DSM in the Second Stage Processing

A further question that was asked is, how much does the use of the DSM improve classification accuracy in the second stage processing? To investigate this, the segmentation technique described in Sec. 5.3 was applied. This began by classifying the whole binary flooded image output from the NN using adjacent 7×7 windows that were overlapping with a stride of 1 pixel, with only the central pixel of a window being required to lie in the urban area. Each pixel in the classified image covered about 70×70 m. To increase the resolution back to that of Sentinel-1,

Table 5 Comparison of test set accuracies using UFI and NN methods.

Site	Test set size	Test set accuracy using UFI (*ufi_thresh* = 3.0)	True flooded rate (Recall)	False flooded rate	Test set accuracy using NN (with model AK)	True flooded rate (recall)	False flooded rate
Aqqala	156	0.83	0.82	0.16	0.85	0.82	0.13
Koriyama	124	0.88	0.81	0.06	0.90	0.83	0.05

the 12-m WorldDEM DSM was used. Provided the highest boundary segment in a flooded region did not intersect the edge of the urban area, the DSM also allowed flood depth to be estimated from flood extent by intersecting the flood extent with the DTM.

As well as using the DSM to improve classification in the second stage processing, it was also used at this stage to improve the validation data for Koriyama and Iwaki. For these sites, the validation data provided were flood extents that assumed the whole extent was covered by water. However, this ignored the fact that the upper parts of many buildings might be emergent. An estimate of these could be made from other validation data available for a site, such as aerial photos and other SAR data, which were used to calculate an approximate flood level independent of that estimated in the second stage processing to identify emergent buildings.

The whole image classification output by the NN was processed by the region segmenter. To assess the increase in accuracy due to the DSM, the accuracy of the modified classification output by the segmenter was estimated with and without using the DSM. For the case without using the DSM, only the steps in the region segmenter up to and including region labeling were performed. Using the Aqqala site as an example, Fig. 12 shows the binary flood classification from the NN, the image output by the region segmenter without using the DSM, and the output from the segmenter using the DSM. The notable feature using the DSM is the identification of the tops of buildings as unflooded, which especially for Aqqala results in the identification of the street structure in the output [Fig. 12(c)].

Figure 13 compares, for each site, the classified whole image with the relevant validation data, with and without using the DSM. For the classifications made without using the DSM, it is apparent that many falsely flooded pixels are occurring at buildings and ground areas above the flood. For the classifications made using the DSM, false flooded pixels are much less.

Figure 14 shows the flood depth maps for the Aqqala, Koriyama, and Blessem floods produced using the DSM. For Aqqala [Fig. 14(a)], flood depth increases to the north. For Koriyama [Fig. 14(b)], an area of deep flooding has been identified. No flood depth map was produced for the Iwaki flood because of the intersection of flood region boundaries with the urban edges.

Table 6 summarizes the classification results for the whole images for all sites. For Aqqala, there is a rise in classification accuracy from 0.79 without the DSM to 0.89 when the DSM is used. For Koriyama, there is a similar rise from 0.89 to 0.94 using the DSM. However, note that the recall using the DSM is only 0.72, because flooding in the north of the image present when the Koriyama validation data were acquired was not present on the SAR image acquired on the previous day [false unflooded (green) area on Fig. 13(d)]. For Iwaki, there is again an accuracy rise from 0.82 to 0.90 using the DSM, and for Blessem, a rise from 0.48 to 0.88.

The increases in accuracy occur mainly because the false flood rate decreases using the DSM. In turn, these decreases arise because the DSM is being used to improve both the segmenter output and (for Koriyama and Iwaki) the validation map. We can conclude that it is definitely helpful to include the DSM in the classification in this way.

Figure 15(a) shows, for the example of the Aqqala dataset, 2D histograms of normalized brightness ratio and coherence ratio for urban pixels from the whole image classified as flooded or unflooded by the NN. The histograms show the distribution of these variables in the feature

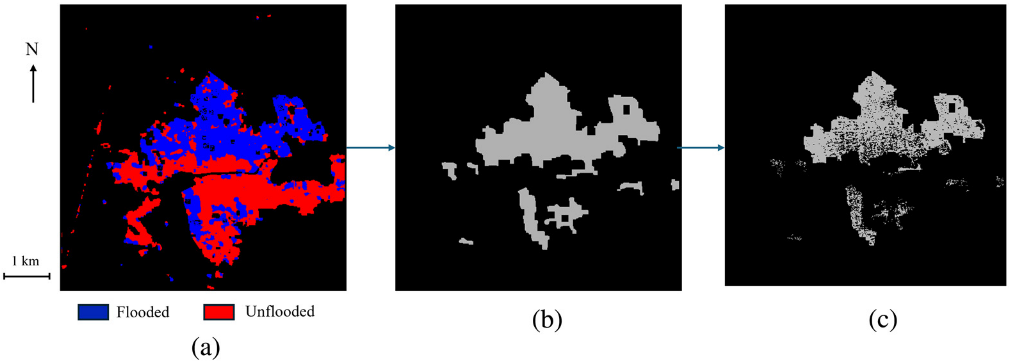

Fig. 12 (a) Aqqala flood map output from neural network, (b) output from region segmenter without using DSM, and (c) output from region segmenter using DSM.

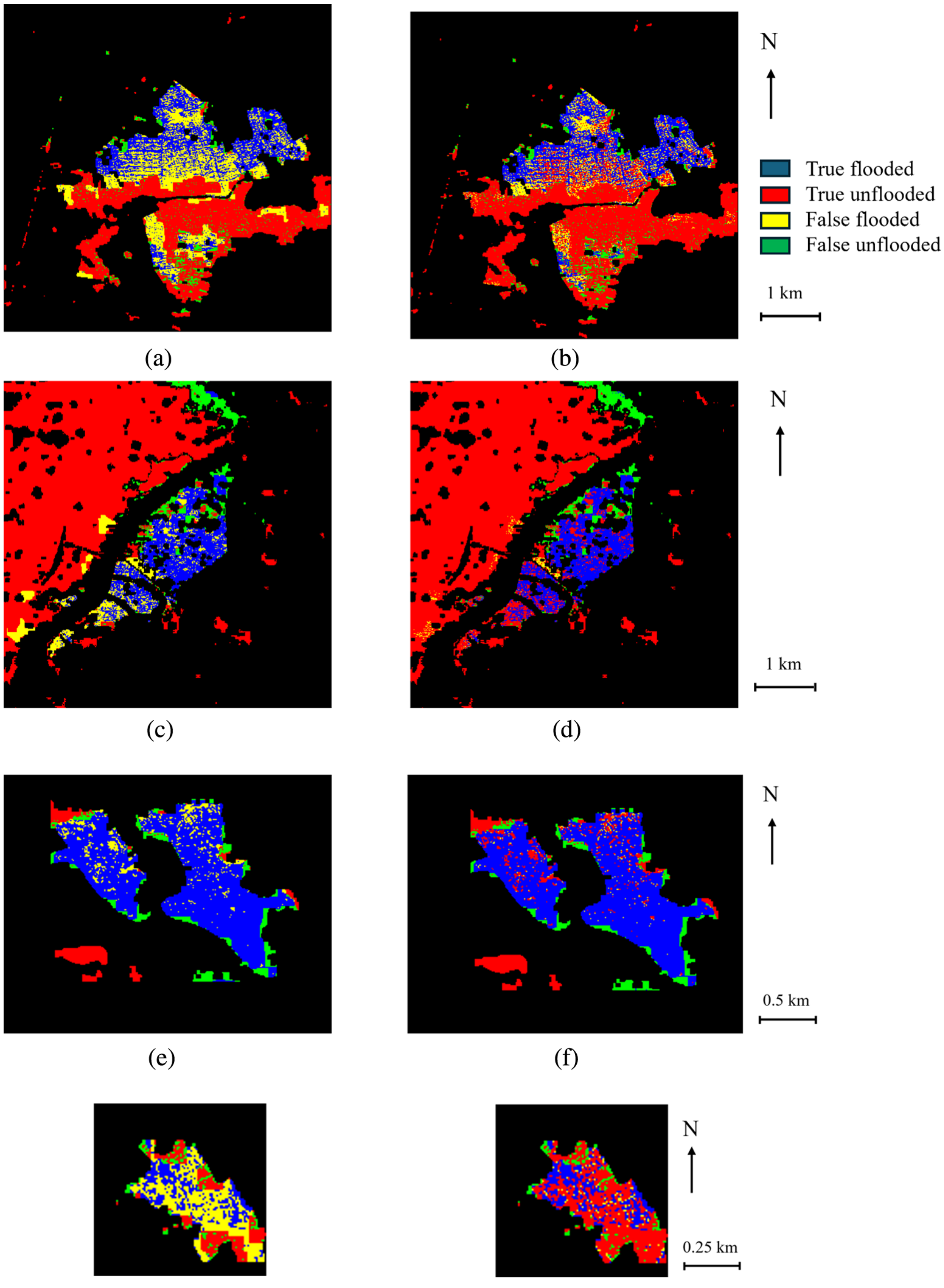

(a) (b)

(c) (d)

(e) (f)

(g) (h)

Fig. 13 Classification in urban area compared with validation data for (a) Aqqala without using DSM, (b) Aqqala using DSM, (c) Koriyama without using DSM, (d) Koriyama using DSM, (e) Iwaki [within yellow rectangle of Fig. 8(e)] without using DSM, (f) Iwaki (within yellow rectangle) using DSM, (g) Blessem without using DSM, and (h) Blessem using DSM.

space for the classifications output from the region segmenter without using the DSM and illustrate the power of the NN at separating flooded pixels from unflooded. As expected, flooded pixels tend to have higher normalized brightness ratios and lower coherence ratios than unflooded ones. For the same dataset, Fig. 15(b) gives the 2D histograms for the classifications output by the region segmenter using the DSM and shows the additional power of the DSM. Many of the pixels classified as flooded in Fig. 15(a) have been reclassified as unflooded in Fig. 15(b). A significant proportion of these tend to have normalized brightness ratios in the

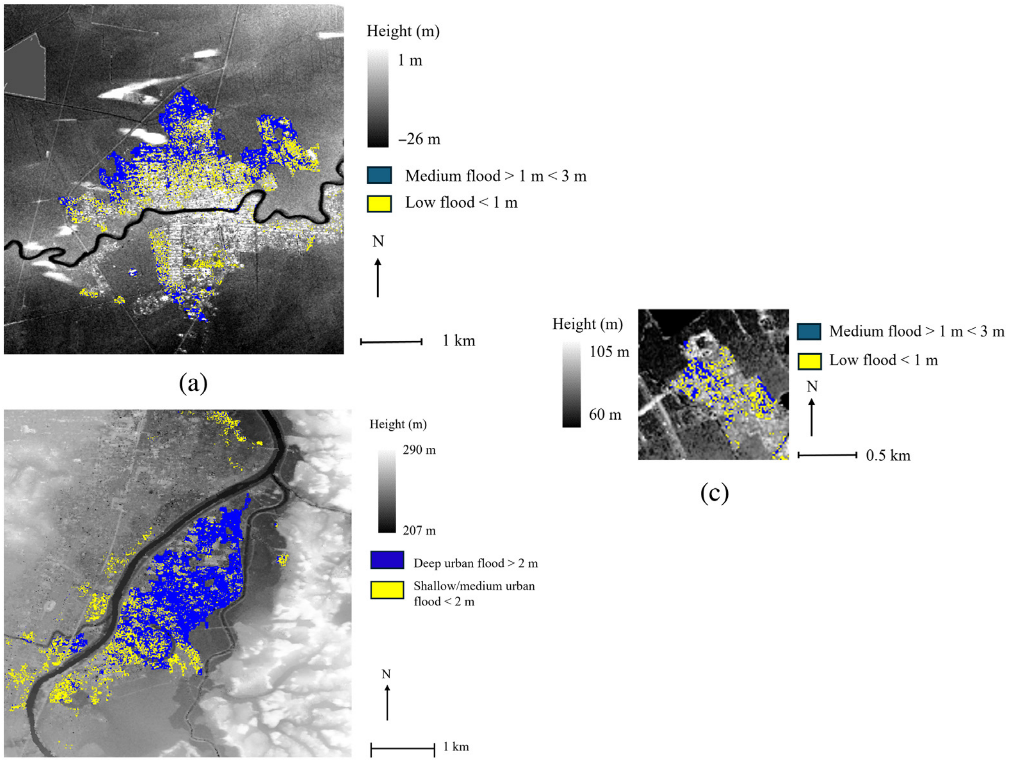

(a)

(b)

(c)

Fig. 14 Flood depth maps for (a) Aqqala, (b) Koriyama, and (c) Blessem.

Table 6 Classification accuracies for whole images for all sites.

Site	Test set size	Accuracy without DSM	True flooded rate (Recall)	False flooded rate	$F1$	Accuracy with DSM	True flooded rate (Recall)	False flooded rate	$F1$
Aqqala	56,418	0.79	0.90	0.27	0.74	0.89	0.82	0.04	0.82
Koriyama	66,167	0.89	0.73	0.08	0.72	0.94	0.72	0.01	0.80
Iwaki	15,718	0.82	0.88	0.49	0.88	0.90	0.88	0.02	0.93
Blessem	1192	0.48	0.76	0.66	0.50	0.88	0.76	0.07	0.81

range 0.2 to 0.3 and coherence ratios greater than 0.5. They are mainly pixels classed as "falsely flooded" in Fig. 13(a).

7 Discussion

The approach adopted allows the user to classify either on the basis of brightness ratio and coherence or using a DSM in addition to these. The DSM, which would need to have similar resolution to that of Sentinel-1, could be WorldDEM in many parts of the world (which would generally not be open-source), but in many developed countries it could be higher-resolution LiDAR (freely available in the UK).

The study has provided further evidence of the difficulty of obtaining independent spatial data of the flooding with which to validate the SAR flood map. Only in one case (Aqqala) has excellent validation data been obtained that is truly contemporaneous with the SAR postflood image. For the other flood events, the validation data available is a mix of the external boundary of the maximum flood extent achieved during the flood and (except for Iwaki) aerial

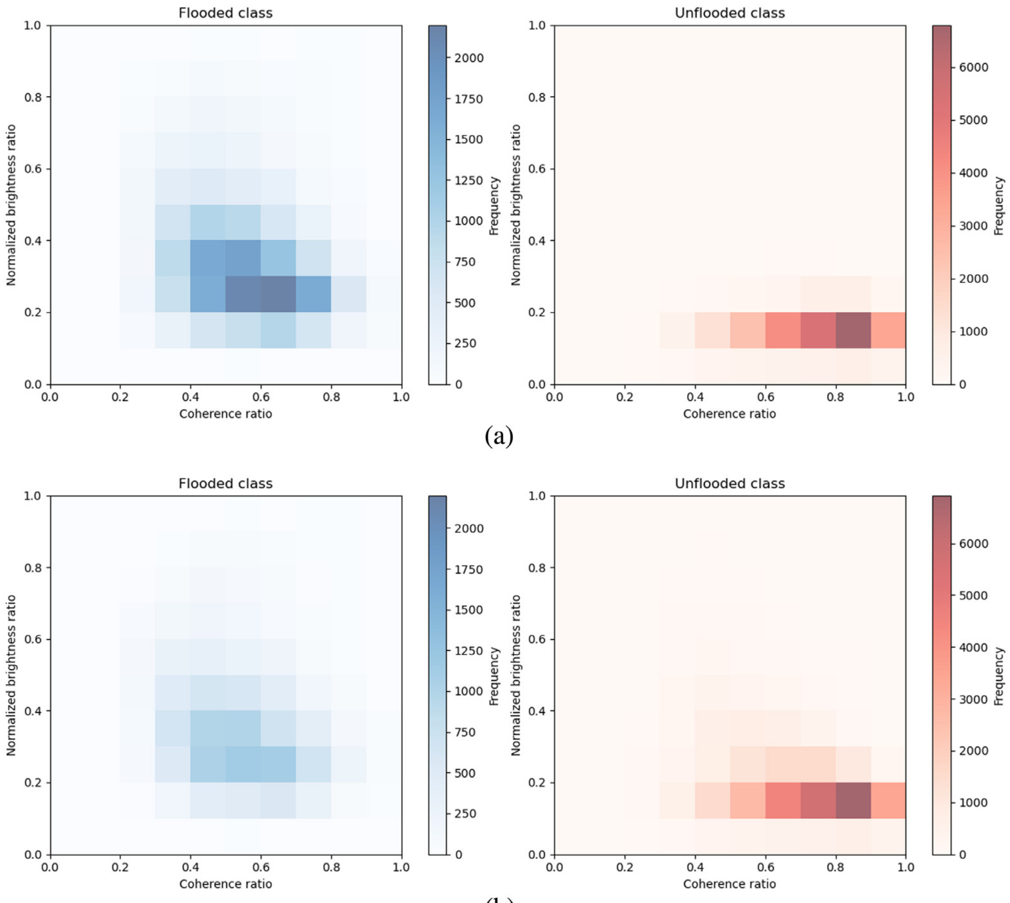

(a)

(b)

Fig. 15 2D histograms of normalized brightness ratio and coherence ratio for the classifications of the Aqqala dataset output from the region segmenter (a) without using the DSM and (b) using the DSM.

photography. This is understandable considering the difficulty of performing a largely ground-based survey, as in the Koriyama and Iwaki cases. As a result, the flood wave at the time of the SAR postflood overpass may have a flood extent that is slightly different from the maximum flood extent (significantly different in the case of Iwaki). Furthermore, the external boundary of the maximum flood extent may also be an overestimate of the flooding, because in the majority of floods, not all buildings will be totally submerged; some of the taller ones will be emergent. A further advantage of using a DSM is that it can help identify these and improve the validation classification for better comparison with the SAR flood map produced using a DSM. If aerial photos are available that are contemporaneous with the SAR postflood overpass, these can be used to assess an approximate flood height using the DSM, which can be used to improve the validation.

The NN model has been constructed from labeled reference data from Aqqala and Koriyama. If further urban floods were imaged for which there were reference data, they could be used to refine the model. However, as noted above, the collection of labelled samples in urban flood images is generally difficult, expensive, and time-consuming. If (as is more likely) further flooding was imaged for which there was no reference data, the unlabeled data might still be used to update the model using machine learning techniques such as semisupervised learning or domain adaptation. Semisupervised learning combines a small amount of labeled data with a generally larger amount of unlabeled data during training.[62] The existing model is used to generate “pseudolabels” for the unlabeled data. The most confident pseudolabels are added to the labeled dataset, and the model is retrained. This expands the labeled dataset and improves the model’s ability to generalize. Alternatively, domain adaptation could be used in situations where there were shifts in distribution between the flood data used for training and those used for testing, which often happens with real-world data.[63] Domain adaptation techniques attempt to align the feature distributions of training and test data to better generalize the model to both data sets.

Due to the limited training data available, the method developed here is a relatively straightforward one employing only shallow learning, in comparison to the sophisticated deep learning approaches employed in Refs. 33–35. However, it is interesting to note that, for the Koriyama urban flooding event, if the whole image is classified using NN with brightness ratio and coherence ratio but not the DSM, our results ($F1 = 0.72$, recall = 0.73, precision = 0.71) compare favourably with those of Ref. 33 (for flooded urban, $F1 = 0.51$, recall = 0.40, precision = 0.71), with the proviso that we have simplified the problem by detecting only urban flooding.

8 Conclusion

The main conclusions from this study are that good classification accuracy can be achieved using brightness ratio and coherence ratio in a neural network and that it is definitely helpful to include the DSM in the classification. The results indicated that using the NN employing only double scattering and coherence, a weighted average classification accuracy/$F1$ value of 84%/0.74 could be achieved on test data. If the DSM was also included in the classification, the weighted average accuracy/$F1$ value increased to 91%/0.82, spatial resolution improved, and flood depth maps could generally be generated.

The findings of this study should be of use in automating the detection of urban flooding as an aid to operational flood incident management and urban flood forecasting.

Disclosures

The authors have no competing interests to declare.

Code and Data Availability

The Sentinel-1 data used in the study are open access,[64] as are the World Settlement Footprint data.[59] The WorldDEM data were purchased from Apollo Mapping.

Acknowledgments

This work was supported by the UK Natural Environment Research Council (NERC Grant No. NE/X019071/1, "UK EO Climate Information Service"). Thanks are due to Remy Vandaele and Varun Ojha for helpful discussions.

References

1. H. Ritchie et al., "Natural disasters," https://ourworldindata.org/natural-disasters (2014).
2. D. Dodman et al., "Climate change 2022: impacts, adaptation and vulnerability. Contribution of working group II to the sixth assessment report of the intergovernmental panel on climate change," Cambridge University, Tech. Rep. (2022).
3. Munich RE, "Loss events worldwide 1980-2014, 10 costliest floods ordered by overall losses," https://www.munichre.com/natcatservice (2015).
4. H. Winsemius et al., "Global drivers of future river flood risk," *Nat. Clim. Change* **6**, 381–385 (2015).
5. B. Tellman et al., "Satellite imaging reveals increased proportion of population exposed to floods," *Nature* **596**(7870), 80–86 (2021).
6. M. Pitt, "Learning lessons from the 2007 floods," U.K. Cabinet Office Report, http://archive.cabinetoffice.gov.uk/pittreview/thepittreview.html (2008).
7. J. Garcia-Pintado et al., "Satellite-supported flood forecast in river networks: a real case study," *J. Hydrol.* **523**, 706–724 (2015).
8. E. S. Cooper et al., "Observation operators for assimilation of satellite observations in fluvial inundation forecasting," *Hydrol. Earth Syst. Sci.* **23**, 2541–2559 (2019).
9. H. Hooker et al., "A multi-system comparison of forecast flooding extent using a scale-selective approach," *Hydrol. Res.* **54**(10), 1115–1133 (2023).
10. H. Hooker et al., "Assessing the spatial spread–skill of ensemble flood maps with remote-sensing observations," *Nat. Hazards Earth Syst. Sci.* **23**(8), 2769–2785 (2023).
11. H. Hooker et al., "Spatial scale evaluation of forecast flood inundation maps," *J. Hydrol.* **612**, 128170 (2022).

12. Copernicus Data Space Ecosystem, "Sentinel-1," EC, 2026, https://dataspace.copernicus.eu/explore-data/data-collections/sentinel-data/sentinel-1 (accessed 5 April 2026).
13. Copernicus, "GloFAS Global Flood Monitoring (GFM)," EC, 2021 , https://www.globalfloods.eu/technical-information/glofas-gfm/ (2021) (accessed 5 April 2026).
14. G. Franceschetti, A. Iodice, and D. Riccio, "A canonical problem in electromagnetic backscattering from buildings," *IEEE Trans. Geosci. Remote Sens.* **40**(8), 1787–1801 (2002).
15. D. C. Mason et al., "Flood detection in urban areas using TerraSAR-X," *IEEE Trans. Geosci. Remote Sens.* **48**(2), 882–894 (2010).
16. D. C. Mason et al., "Near real-time flood detection in urban and rural areas using high resolution synthetic aperture radar images," *IEEE Trans. Geosci. Remote Sens.* **50**(8), 3041–3052 (2012).
17. D. C. Mason et al., "Detection of flooded urban areas in high resolution Synthetic Aperture Radar images using double scattering," *Int. J. Appl. Earth Obs. Geoinf.* **28**, 150–159 (2014).
18. M. Tanguy et al., "River flood mapping in urban areas combining RADARSAT-2 and flood return period data," *Remote Sens. Environ.* **198**, 442–459 (2017).
19. L. Giustarini et al., "A change detection approach to flood mapping in urban areas using TerraSAR-X," *IEEE Trans. Geosci. Remote Sens.* **51**(4), 2417–2430 (2013).
20. P. Iervolino et al., "Flooding water depth estimation with high-resolution SAR," *IEEE Trans. Geosci. Remote Sens.* **53**(5), 2295–2307 (2015).
21. D. C. Mason, S. L. Dance, and H. L. Cloke, "Floodwater detection in urban area using Sentinel-1 and WorldDEM data," *J. Appl. Remote Sens.* **15**(3), 032003 (2021).
22. Z. Wang et al., "Combining SAR images with land cover products for rapid urban flood mapping," *Front. Environ. Sci.* **10**, 973192 (2022).
23. M. T. Islam and Q. Meng, "An exploratory study of Sentinel-1 SAR for rapid urban flood mapping on Google Earth Engine," *Int. J. Appl. Earth Obs. Geoinf.* **113**, 103002 (2022).
24. Q. Yang et al., "Promoting SAR-based urban flood mapping with adversarial generative network and out of distribution detection," in *Proc. IGARSS*, pp. 2336–2338 (2023).
25. L. Pulvirenti et al., "Use of SAR data for detecting floodwater in urban and agricultural areas: the role of interferometric coherence," *IEEE Trans. Geosci. Remote Sens.* **54**(3), 1532–1544 (2016).
26. M. Chini et al., "Sentinel-1 InSAR coherence to detect floodwater in urban areas: Houston and Hurricane Harvey as a test case," *Remote Sens.* **11**(2), 107 (2019).
27. Y. Li et al., "Urban flood mapping using SAR intensity and interferometric coherence via Bayesian network fusion," *Remote Sens.* **11**(19), 2231 (2019).
28. Y. Li, S. Martinis, and M. Wieland, "Urban flood mapping with an active self-learning convolutional neural network based on TerraSAR-X intensity and interferometric coherence," *ISPRS J. Photogramm. Remote Sens.* **152**, 178–191 (2019).
29. I. Olthof and N. Svacina, "Testing urban mapping approaches from satellite and in-situ data collected during 2017 and 2019 events in Eastern Canada," *Remote Sens.* **12**(19), 3141 (2020).
30. A. Bioretsita, N. Hayati, and M. G. R. Ngurawan, "Integrating InSAR coherence and backscattering for identification of temporary surface water, case study: South Kalimantan flooding, Indonesia," *Int. Arch. Photogramm. Remote Sens. Spatial Inf. Sci.* **XLIII-B3-2022**, 33–39 (2022).
31. H. Zhang et al., "An urban flooding index for unsupervised inundated urban area detection using Sentinel-1 polarimetric SAR images," *Remote Sens.* **13**(22), 4511 (2021).
32. R. Pelich et al., "Mapping floods in urban areas from dual-polarization InSAR coherence data," *IEEE Geosci. Remote Sens. Lett.* **19** (2022).
33. J. Zhao et al., "Urban-aware U-Net for large-scale urban flood mapping using multitemporal Sentinel-1 intensity and interferometric coherence," *IEEE Trans. Geosci. Remote Sens.* **60**, 4209121 (2022).
34. N. G. Sorboni et al., "Urban flood mapping using Sentinel-1 and RADARSAT constellation mission image and convolutional Siamese network," *Nat. Hazards* **120**, 5711–5742 (2024).
35. J. Zhao et al., "Urban SARFloods: Sentinel-1 SLC-based benchmark dataset for urban and open-area flood mapping," in *Proc. CVPR 2024 EarthVision Workshop*, pp. 419–429 (2024).
36. L. Pulvirenti et al., "Flood detection in urban areas: analysis of time series of coherence data in stable scatterers," in *Proc. IGARSS*, pp. 9745–9747 (2019).
37. L. Pulvirenti, M. Chini, and N. Pierdicca, "InSAR multitemporal data over persistent scatterers to detect floodwater in urban areas: a case study in Beletweyne, Somalia," *Remote Sens.* **13**(1), 37 (2021).
38. L. Moya et al., "Learning from the 2018 Western Japan Heavy Rains to detect floods during the 2019 Hagibis Typhoon," *Remote Sens.* **12**(14), 2244 (2020).
39. J. Zhao et al., "Urban flood mapping using satellite synthetic aperture radar: a review of characteristics, approaches and datasets," arXiv:2411.04153v1 (2024).
40. G. Gnan et al., "Improved building-specific flood risk assessment and implications of depth-damage function selection," *Front. Water* **4**, 919726 (2022).

41. Copernicus Data Space Ecosystem, "Copernicus DEM - Global and European Digital Elevation Model," EC, https://dataspace.copernicus.eu/explore-data/data-collections/copernicus-contributing-missions/collections-description/COP-DEM (accessed 5 April 2026).
42. Environment Agency, "National LIDAR Programme," UK EA, 2025,https://www.data.gov.uk/dataset/f0db0249-f17b-4036-9e65-309148c97ce4/national-lidar-programme (accessed 5 April 2026).
43. D. C. Mason, S. L. Dance, and H. L. Cloke, "Towards improved urban flood detection using Sentinel-1: dependence of the ratio of post- to pre-flood double scattering cross-sections on building orientation," *J. Appl. Remote Sens.* **17**(1), 016507 (2023).
44. D. C. Mason and S. L. Dance, "Improved urban flood detection in deeper floods using synthetic aperture radar double scattering intensity and interferometric coherence," *J. Appl. Remote Sens.* **19**(2), 021007 (2025).
45. G. Franceschetti et al., "SAR raw signal simulation for urban structures," *IEEE Trans. Geosci. Remote Sens.* **41**(9), 1986–1995 (2003).
46. M. Motlagh, "Aerial photos of Aqqala devastating flood," https://en.mehrnews.com/photo/143596/Aerial-photos-of-Aqqala-devasting-flood (2019).
47. K. Ganji et al., "Urban's river flood analysing using Sentinel-1 data case study: (Gorganrood, Aq'qala)," *Int. Arch. Photogramm. Remote Sens. Spatial Inf. Sci.* **XLII-4/W18**, 415–419 (2019).
48. S. K. McFeeters, "The use of the normalized difference water index (NDWI) in the delineation of open water features," *Int. J. Remote Sens.* **17**(7), 1425–1432 (1996).
49. H. Farhadi et al., "Near real-time flood monitoring using multi-sensor optical imagery and machine learning by GEE: an automatic feature-based multi-class classification approach," *Remote Sens.* **16**(23), 4454 (2024).
50. Geospatial Information Authority of Japan, "Information about typhoon no. 19," https://www.gsi.go.jp/BOUSAI/R1.taihuu19gou.html (2019).
51. Synspective, "Analysing the Abukuma River Flood (2019) with Flood Damage Assessment," Synspective, 2020, https://www.theguardian.com/world/gallery/2019/oct/14/the-aftermath-of-typhoon-hagibis-in-pictures (accessed 5 April 2026).
52. JBA, "Typhoon Hagibis: JBA Risk Management event response, 14 October 2019," https://www.jbarisk.com/products-services/event-response/typhoon-hagibis/ (2019).
53. Synspective, "Analysing the Abukuma river flood (2019) with flood damage assessment," https://synspective.com/usecase/2020/fda1/ (2020).
54. Iwaki City, "Flood damage debris removal enhancement period," http://www.city.iwaki.lg.jp/www/contents/1572477821789/simple/1030.pdf (2019).
55. Google Earth Pro, Iwaki, Japan. 37°05′13″N, 140°52′35″E, eye alt 6.97 km. Image © 2025 Maxar Technologies, https://earth.google.com/web/ (2025).
56. Guardian, "'It's all wrecked': German town stunned by flood damage," Guardian, 2021, https://mapping.emergency.copernicus.eu/activations/EMSR517/ (accessed 5 April 2026).
57. Copernicus Emergency Management Service, "Flood in Western Germany," EU, 13 July 2021, https://www.theguardian.com/world/2021/jul/16/all-wrecked-german-town-stunned-flood-damage (accessed 5 April 2026).
58. ESA, "Sentinel-1 Toolbox: TOPS Interferometry Tutorial", ESA, 2021, https://step.esa.int/docs/tutorials/S1TBX%20TOPSAR%20Interferometry%20with%20Sentinel-1%20Tutorial_v2.pdf (accessed 5 April 2026).
59. ESA, "ESA Urban TEP", ESA, https://urban-tep.eu/#! (2019).
60. M. Ahishali et al., "Dual and single polarized SAR image classification using compact convolutional neural networks," *Remote Sens.* **11**, 1340 (2019).
61. A. Mao et al., "Cross-entropy loss functions: Theoretical analysis and applications," in *Proc. ICML*, pp. 23803–23828 (2023).
62. Z. Yue et al., "A novel semi-supervised convolutional neural network method for synthetic aperture radar image recognition," *Cogn. Comput.* **13**, 795–806 (2019).
63. A. Farahani et al., "A brief review of domain adaptation," in *Advances in Data Science and Information Engineering*, R. Stahlbock et al., Eds., Trans. Comp. Sci. Comp. Intell., pp. 877–886, Springer, Switzerland, Cham (2021).
64. Copernicus Data Space Ecosystem, "Welcome to Copernicus Data Space Ecosystem," EC, https://dataspace.copernicus.eu/ (2023).

David C. Mason is a postdoctoral research assistant attached to the National Center for Earth Observation in the Department of Meteorology at the University of Reading, UK. He obtained his BSc and PhD in physics from Imperial College, University of London. His current research interest is the use of remote sensing in hydrology, in particular, using SAR flood extents for emergency flood relief management and improved flood inundation forecasting.

Sarah L. Dance is professor of data assimilation at the University of Reading, UK, jointly held in the Department of Mathematics and Statistics and the Department of Meteorology. She completed her PhD in the Division of Applied Mathematics at Brown University, USA, in 2002. Her research interests span mathematical and applied developments in data assimilation and the use of observations, particularly for hazardous weather and flooding.